toxins

Article

# Electrospun Membranes Anchored with g-$C_3N_4$/$MoS_2$ for Highly Efficient Photocatalytic Degradation of Aflatoxin $B_1$ under Visible Light

**Ruixin Song [1,†], Liangtao Yao [1,†], Changpo Sun [2], Dechao Yu [1], Hui Lin [1], Guisheng Li [3], Zichao Lian [3], Songlin Zhuang [1,*] and Dawei Zhang [1,4,*]**

1 Engineering Research Center of Optical Instrument and System, Ministry of Education and Shanghai Key Lab of Modern Optical System, University of Shanghai for Science and Technology, No. 516 Jungong Road, Shanghai 200093, China
2 Standards and Quality Center of National Food and Strategic Reserves Administration, No. 25 Yuetan North Street, Xicheng District, Beijing 100834, China
3 Department of Chemistry, College of Science, University of Shanghai for Science and Technology, No. 516 Jungong Road, Shanghai 200093, China
4 Fujian Provincial Key Laboratory for Advanced Micro-Nano Photonics Technology and Devices, Research Center for Photonics Technology, Quanzhou Normal University, Quanzhou 362046, China
* Correspondence: slzhuang@yahoo.com (S.Z.); dwzhang@usst.edu.cn (D.Z.)
† These authors contributed equally to this work.

**Abstract:** The degradation of aflatoxin (AF) is a topic that always exists along with the food and feed industry. Photocatalytic degradation as an advanced oxidation technology has many benefits, including complete inorganic degradation, no secondary contamination, ease of activity under moderate conditions, and low cost compared with traditional physical, chemical, and biological strategies. However, photocatalysts are usually dispersed during photocatalytic reactions, resulting in energy and time consumption in the separation process. There is even a potential secondary pollution problem from the perspective of food safety. In this regard, three electrospun membranes anchored with g-$C_3N_4$/$MoS_2$ composites were prepared for highly efficient photocatalytic degradation of aflatoxin $B_1$ ($AFB_1$) under visible light. These photocatalytic membranes were characterized by XRD, SEM, TEM, FTIR, and XPS. The factors influencing the degradation efficiency of $AFB_1$, including pH values and initial concentrations, were also probed. The three kinds of photocatalytic membranes all exhibited excellent ability to degrade $AFB_1$. Among them, the photocatalytic degradation efficiency of the photocatalytic membranes prepared by the coaxial methods reached 96.8%. The experiment is with an initial concentration of 0.5 μg/mL (500 PPb) after 60 min under visible light irradiation. The mechanism of degradation of $AFB_1$ was also proposed based on active species trapping experiments. Moreover, the prepared photocatalytic membranes exhibited excellent photocatalytic activity even after five-fold use in the degradation of $AFB_1$. These studies showed that electrospun membranes anchored with g-$C_3N_4$/$MoS_2$ composites have a high photocatalytic ability which is easily removed from the reacted medium for reuse. Thereby, our study offers a highly effective, economical, and green solution for $AFB_1$ degradation in the foodstuff for practical application.

**Keywords:** electrospun photocatalytic membranes; aflatoxin $B_1$; flexible; visible light; g-$C_3N_4$/$MoS_2$

**Key Contribution:** The flexible electrospun membranes anchored with g-$C_3N_4$/$MoS_2$ composites were synthesized via the uniaxial or coaxial electrospinning technique, and showed excellent ability to degrade $AFB_1$ by the synergism of adsorption and photocatalysis under visible light irradiation. The prepared photocatalytic membranes had good mechanical properties and were easy to separate from the $AFB_1$ solution, and the mechanisms of adsorption and photodegradation of $AFB_1$ were revealed.

check for updates

**Citation:** Song, R.; Yao, L.; Sun, C.; Yu, D.; Lin, H.; Li, G.; Lian, Z.; Zhuang, S.; Zhang, D. Electrospun Membranes Anchored with g-$C_3N_4$/$MoS_2$ for Highly Efficient Photocatalytic Degradation of Aflatoxin $B_1$ under Visible Light. *Toxins* **2023**, *15*, 133. https://doi.org/10.3390/toxins15020133

Received: 18 January 2023
Revised: 1 February 2023
Accepted: 2 February 2023
Published: 6 February 2023

## 1. Introduction

Aflatoxin $B_1$ ($AFB_1$) is a highly toxic mycotoxin produced by aspergillus species as secondary metabolites under specific conditions [1–3]. It can contaminate food in a variety of ways and get into the human food chain directly or indirectly, threatening human health because of its genetic toxicity, carcinogenesis, embryonic toxicity, teratogenic, and immunotoxicity [4,5]. Studies have shown that a large amount of $AFB_1$ consumed quickly can cause liver damage, such as acute hepatitis and liver tissue hemorrhage. Long-term intake of $AFB_1$ can lead to chronic poisoning symptoms, such as liver fibrosis, poor growth, infertility, fetal malformation, etc. [6]. The International Agency for Research on Cancer (IARC) has listed $AFB_1$ as a type I carcinogen [7–10]. In order to ensure human health and safety, the maximum allowable limits of $AFB_1$ in various foods are determined. In the European Commission, the maximum allowable limit of $AFB_1$ in edible oil, grain, and cereal products is 2 μg/kg. In China, the maximum allowable limit of $AFB_1$ in peanut and corn oil is 20 μg/kg, while that in other vegetable oils is 10 μg/kg. In the United States, the maximum allowable limit of total aflatoxin ($AFB_1$ + $AFB_2$ + $AFG_1$ + $AFG_2$) in foods is 20 μg/kg. Meanwhile, animals fed with feed contaminated by $AFB_1$ for a long time will increase the probability of disease and reduce feed conversion efficiency [11,12].

Various approaches have been reported for the detoxification of $AFB_1$, including physical, chemical, and biological treatments. The most common physical detoxification method uses adsorbents in which $AFB_1$ can be adsorbed during the process of detoxification [13,14]. Although many adsorbents, such as diatomite and montmorillonite, are used in practical applications, some common drawbacks include poor adsorptive efficiency, weak selectivity, high-cost recyclability, and even non-renewability. Chemical detoxification methods mainly use chlorine dioxide, ozone, sodium hypochlorite, and other chemicals to degrade $AFB_1$ [15,16]. However, the problem of chemical residues has not been effectively solved and may cause secondary pollution. Another approach is to employ biodegradable enzymes or microorganisms to decompose $AFB_1$ [17,18]. However, the application of the biological method is limited because the enzyme or bacteria agents are sensitive to environmental temperature, humidity, pH value, and the cost is high. Moreover, the increasing concern about food safety and the quality of the environment has prompted researchers to seek an efficient, safe, rigorous, and affordable technology to degrade $AFB_1$.

Photocatalytic technology was developed in the 1970s [19] and is increasingly used in mycotoxins' degradation [20–22]. In a photocatalytic reaction, when light with appropriate energy ($h\nu \geq E_g$) falls on photocatalytic materials, electrons ($e^-$) get excited from the valence band (VB) to the conduction band (CB), leaving behind holes ($h^+$). Then, these photogenerated charges ($e^-$ and $h^+$) migrate from the inside to the surface of the photocatalyst and interact with $O_2$, $H_2O$, or $OH^-$ around to produce $\bullet O_2^-$ and $\bullet OH$ with strong oxidation, which can degrade $AFB_1$ and convert it into less hazardous compounds such as small organic acids, $CO_2$, or $H_2O$ [23,24]. Compared with the physical, chemical, and biological treatments mentioned above, detoxifying mycotoxins using a photocatalytic approach is an emerging and promising strategy because of several advantages, including being free from secondary pollution, having mild conditions, and being economical, highly efficient, and environmental-friendly. Different studies have been carried out for detoxifying mycotoxin, including $AFB_1$ and deoxynivalenol (DONs), using photocatalytic technology (Table 1). Recently, by using the experiments of isotope tracing, electron spin resonance, and active species trapping, Mao et al. found that preferentially inactivating the C8=C9 site by the addition reaction of hydroxyl radical was the main pathway for the detoxification of aflatoxin B1 [22]. Furthermore, hydroxyl radicals were most likely to react with the C9 site and then form $AFB_1$-9-hydroxy through oxidative addition reaction, which was verified by theoretical calculations.

**Table 1.** Studies have reported the photocatalytic detoxification of mycotoxin.

| Pollutant (Concentration) | Medium | Catalyst | Source | Time | Degradation | Ref (Year) |
|---|---|---|---|---|---|---|
| $AFB_1$ (0.5 μg/mL) | Aqueous | g-$C_3N_4$ (0.1 mg/mL) | Xenon lamp (300 W, λ ≥ 400 nm) | 120 min | 70.20% | [23] Mao et al. (2018) |
| $AFB_1$ (0.54 μg/mL) | Aqueous | $WO_3$/RGO /g-$C_3N_4$ (0.1 mg/mL) | Xenon lamp (300 W, λ ≥ 420 nm) | 120 min | 92.40% | [25] Mao et al. (2018) |
| $AFB_1$ (0.426 μg/mL) | Aqueous | $WO_3$/CdS | Visible light irradiation (λ ≥ 420 nm) | 80 min | 95.50% | [22] Mao et al. (2019) |
| $AFB_1$ (0.5~2 μg/mL) | Methanol | AC/$TiO_2$ (0.3 mg/mL) | Mercury lamp (130 W, 350–450 nm) | 120 min | 98% | [26] Sun et al. (2019) |
| $AFB_1$ (0.5 μg/mL) | Aqueous | $TiO_2$ /UiO-67 (0.1 mg/mL) | Xenon lamp (300 W, λ ≥ 420 nm) | 80 min | 98.90% | [27] Zhang et al. (2022) |
| $AFB_1$ (0.5~30 μg/mL) | Aqueous/ Soymilk | ZnO, $Fe_2O_3$, $MnO_2$ and CuO (0.1 mg/mL) | UV irradiation | 60 min | ±95% | [28] Raesi et al. (2022) |
| $AFB_1$/$AFB_2$/ $AFG_1$/$AFG_2$ (315.21 μg/kg) | Peanuts | g-$C_3N_4$ /$NiFe_2O_4$ (2 mg/mL) | Xenon lamp (300 W, λ ≥ 420 nm) | 90 min | 94.10% | [29] Sun et al. (2021) |
| DONs (15 μg/mL) | Aqueous | Graphene /ZnO (0.5 mg/mL) | UV irradiation | 120 min | 99.00% | [20] Sun et al. (2017) |
| DONs (4 μg/mL) | Aqueous | α-$Fe_2O_3$ (0.1 mg/mL) | Xenon lamp (300 W, λ ≥ 420 nm) | 120 min | 90.30% | [30] Mao et al. (2019) |

When the photocatalysts mentioned above were used to degrade $AFB_1$ and DONs, the photocatalysts were generally suspended during the photocatalytic process [22–29]. As a result, the photocatalyst powders were easy to agglomerate and the separation process after the photocatalytic reaction required a lot of energy, which limited its large-scale application [31]. It is an attractive solution to prepare membranes by electrospinning as the carrier of photocatalysts. Electrospinning can produce fibers of tens to hundreds of nanometers in diameter with good mechanical properties, which can easily immobilize and recycle photocatalysts [32,33]. Thus, the energy consumption in the separation process and possible secondary pollution are reduced. Up to now, we have not found any reports on photocatalytic degradation of $AFB_1$ using photocatalysts immobilized on electrospun membranes.

$AFB_1$ is often produced during the storage, transportation, and production of foods or food ingredients [2,3]; so, the safety and stability of photocatalysts must be considered. Among the numerous photocatalysts, graphitic carbon nitride (g-$C_3N_4$) has gained the intensive attention of many researchers, as this metal-free polymeric n-type semiconductor is non-toxic, chemically stable, thermally stable, and easily modified [34]. However, the pristine g-$C_3N_4$ is usually restricted by unsatisfactory photocatalytic efficiency due to insufficient solar light absorption and the fast recombination of photogenerated electron–hole pairs [35]. In order to improve the photocatalytic efficiency of g-$C_3N_4$, it is a reasonable strategy to construct heterostructures with other narrow-band gap semiconductors to provide more active sites and inhibit the recombination of photogenerated charges. Molybdenum disulfide ($MoS_2$) consists of three-dimensional stacked atomic layers with direct and indirect band gaps of 1.90 eV and 1.20 eV. It has become one of the most popular emerging co-catalysts due to its appropriate band structure, low cost, non-toxic, and exhibits excellent sunlight harvesting capability [36]. Therefore, it is a good idea to composite g-$C_3N_4$ with $MoS_2$ to form effective heterostructures to enhance the visible light absorption and reduce the recombination of photogenerated electron–hole pairs owing to their matching band-edge positions for photocatalytic application [37]. To the best of our knowledge, the attempt to use electrospun membranes anchored with g-$C_3N_4$/$MoS_2$ to degrade $AFB_1$ under visible light irradiation has not been reported.

## 2. Results and Discussion

Based on the above considerations, we prepared g-$C_3N_4$/$MoS_2$ composites by calcination and hydrothermal methods and investigated their photocatalytic properties. Then, the prepared photocatalysts were dispersed in the polymer electrospinning solution synthesized by polyacrylonitrile (PAN), and flexible electrospun membranes with different structures anchored with g-$C_3N_4$/$MoS_2$ composites were prepared by uniaxial and coaxial methods, respectively. The as-prepared photocatalysts and flexible electrospun membranes ($S_1$, $S_2$, and $S_3$) were characterized by scanning electron microscopy (SEM), transmission electron microscopy (TEM), X-ray diffraction (XRD), Fourier-transform infrared spectroscopy (FTIR), X-ray photoelectron spectroscopy (XPS), and diffuse reflectance spectra (DRS). The photocatalytic efficiency of electrospun membranes for degradation of $AFB_1$ under visible light irradiation in an aqueous medium was investigated. Effects of factors such as pH value and the initial concentration of $AFB_1$ were also studied. Active species trapping experiments analyzed the mechanism of photocatalytic degradation of AFB1. In addition, the effect of recycling on photocatalytic efficiency was also evaluated.

### 2.1. Characterization of the PAN-g-$C_3N_4$/$MoS_2$ Electrospun Membranes

To study the morphologies of electrospun membranes anchored with g-$C_3N_4$/$MoS_2$ prepared by different processes, $S_1$, $S_2$, and $S_3$ were examined by SEM (Figure 1). It could be seen spindle-like beads wrapped with g-$C_3N_4$/$MoS_2$ on $S_1$ (Figure 1a), which indicated the photocatalysts were successfully immobilized on electrospun membranes. Many other researchers have prepared a series of photocatalytic membranes by similar methods [38]. However, most of the photocatalysts in this kind of membrane were wrapped by polymers, which hindered light absorption and was not conducive to the migration of photogenerated charges to the active sites. Therefore, polyethylene oxide (PEO) was added into the electrospinning solution, which is very soluble in water, and the obtained electrospun membranes were treated with an ultrasonic water bath to expose more photocatalysts. From the red circles marked (Figure 1b), it could be confirmed that pores formed by removing PEO after post-treatment, so that more photocatalysts were exposed and the photocatalytic efficiency was enhanced accordingly. To further expose the photocatalysts, coaxial electrospinning and ultrasonic water washing treatment were adopted to prepare $S_3$. Compared with $S_1$ and $S_2$, the spindle-like beads were greatly reduced, and the photocatalysts that were completely exposed due to PEO could be obliterated. The way electrospun nanofibers bound the photocatalysts (Figure 1c) and wave-like folds caused by the removal of PEO could be observed in the bright area around the red circle. With the increase in photocatalysts exposure, it can be speculated that the photocatalytic efficiency should be improved correspondingly.

The morphologies of the g-$C_3N_4$/$MoS_2$ composites were further studied by TEM and HRTEM (Figure 2). It was observed that the well-crystallized $MoS_2$ lines were loaded on g-$C_3N_4$ (Figure 2a). Furthermore, many clear lattice fringes were shown in the HRTEM image (Figure 2b), indicating that good crystallinity has been obtained. Three sets of different lattices were found with the d-spacing of 0.62 nm, 0.32 nm, and 0.27 nm, respectively, corresponding to the (002) plane of $MoS_2$, the (002) plane of g-$C_3N_4$, and the (110) plane of $MoS_2$, respectively [39]. Meanwhile, the interface between g-$C_3N_4$ and $MoS_2$ could also be perceived, indicating that the heterostructures were successfully formed between g-$C_3N_4$ and $MoS_2$.

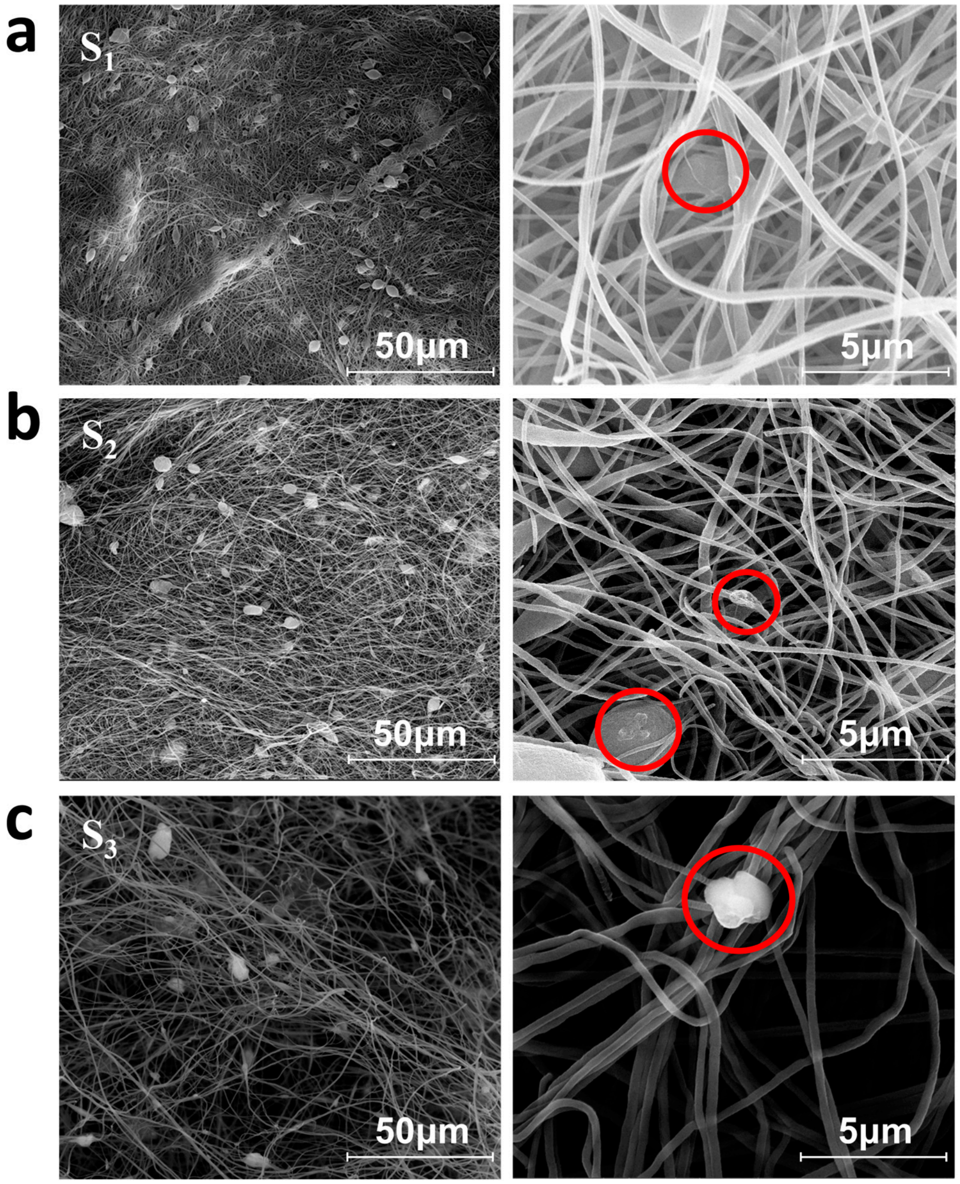


**Figure 1.** SEM images of electrospun membranes anchored with g-$C_3N_4$/$MoS_2$ prepared by different processes: (**a**) $S_1$~mostly wrapped, (**b**) $S_2$~partially exposed, and (**c**) $S_3$~fully exposed.

The crystal structure and composition of g-$C_3N_4$/$MoS_2$, $S_1$, $S_2$, and $S_3$ were confirmed with X-ray diffraction (XRD). In addition, the XRD pattern of g-$C_3N_4$ and $MoS_2$ was displayed to be compared with g-$C_3N_4$/$MoS_2$ (Figure S1), which provided more detailed data. As shown in Figure S1a, several diffraction peaks could be observed at 2θ = 14.5°, 32.8°, 33.66°, 39.68°, 44.32°, and 49.92°, corresponding to (002), (100), (101), (103), (006), and (105) planes of $MoS_2$ (JCPDS: 37-1492), respectively [40]. Compared with the standard card, the diffraction peaks of g-$C_3N_4$/$MoS_2$ and $MoS_2$ shifted slightly to a bigger angle, which might be due to the residual stress in the material [41]. As shown in Figure S1b, the diffraction peak of g-$C_3N_4$, which appeared at 2θ = 13.14°, was assigned to the (001) plane, attributed to the triazine unit, and the strong peak located at 28.02° was the typical (002) diffraction plane ascribed to the inter-planar stacking of the aromatic system in g-$C_3N_4$ (JCPDS: 87-1526) [29]. By contrast, the diffraction peak of g-$C_3N_4$/$MoS_2$ shifted to a smaller angle, implying the interaction between the g-$C_3N_4$ and $MoS_2$. Through the Scherrer formula (Supplementary Information), the crystallite size of g-$C_3N_4$/$MoS_2$ at the (002) plane could be estimated to be 98 Å, more significant than the crystallite size of g-$C_3N_4$

at the (002) plane (88 Å), which might be attributed to the improvement of crystallinity after annealing.

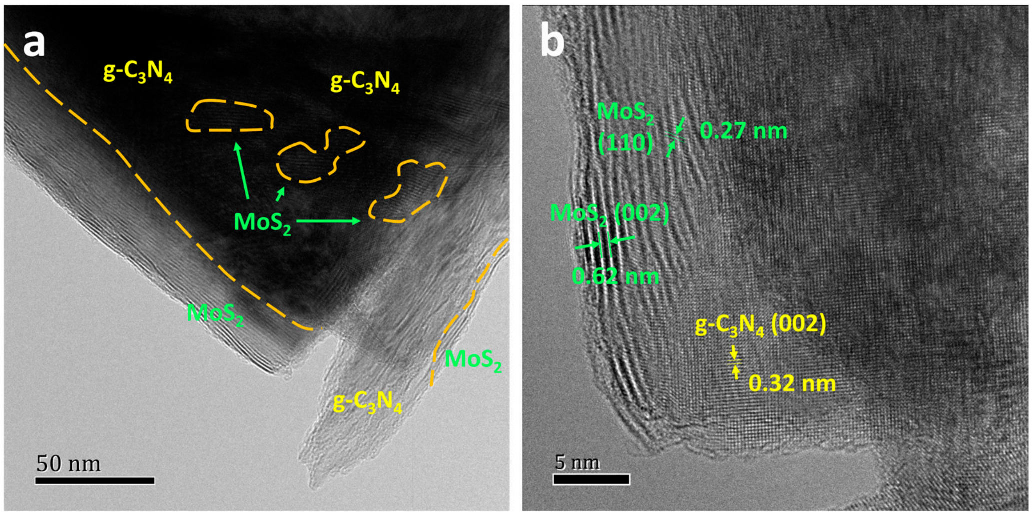


**Figure 2.** (**a**) TEM and (**b**) HRTEM images of g-$C_3N_4$/$MoS_2$ composites.

The XRD patterns of $S_1$, $S_2$, and $S_3$ were generally very similar (Figure 3a) since they were all composed of PAN and g-$C_3N_4$/$MoS_2$. The only difference lay in the spatial structure of the photocatalysts and PAN nanofibers. Obvious diffraction peaks belonging to $MoS_2$ and g-$C_3N_4$ could be observed at 2θ = 14.72° and 27.5° in the XRD patterns of $S_1$, $S_2$, and $S_3$, respectively. Additionally, wide bumps could be observed in the range of 15–30°, similar to the work of Xie et al. [42], representing the amorphous PAN macromolecules. The results of XRD patterns could confirm the successful combination of g-$C_3N_4$/$MoS_2$ composites and PAN electrospun membranes. Other diffraction peaks of g-$C_3N_4$/$MoS_2$ were not found in the XRD patterns of $S_1$, $S_2$, and $S_3$ due to the low content of photocatalysts and the amorphous nature of PAN.

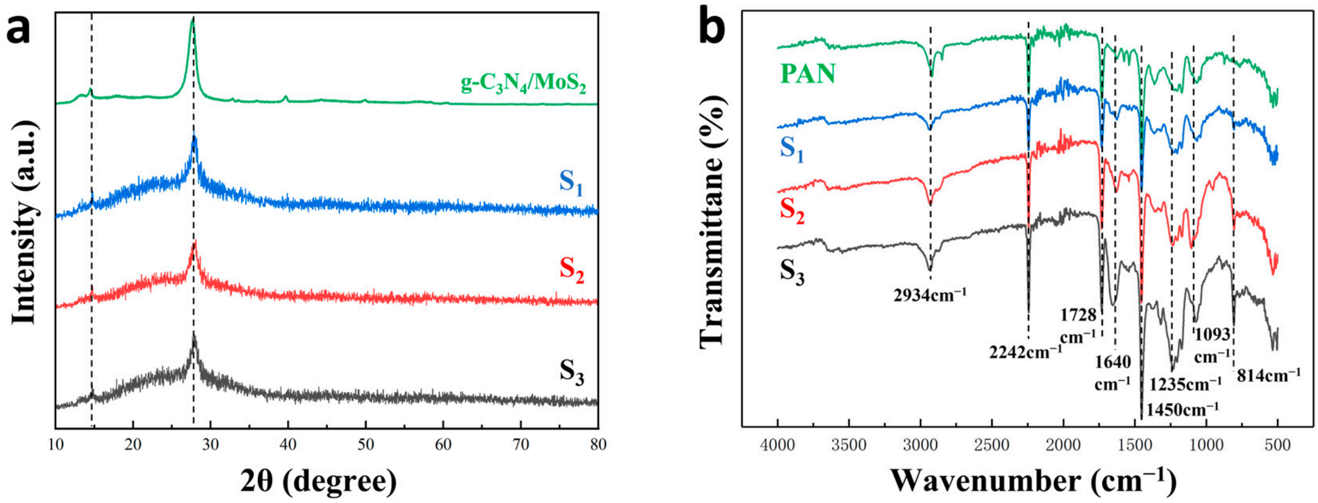


**Figure 3.** (**a**) XRD patterns and (**b**) FTIR spectra of $S_1$, $S_2$, and $S_3$.

The FTIR spectra of the different electrospun membranes were measured (Figure 3b). For pure PAN electrospun membrane, the peaks at 2934 $cm^{-1}$, 2242 $cm^{-1}$, 1728 $cm^{-1}$, 1450 $cm^{-1}$, and 1093 $cm^{-1}$ were assigned to the stretching vibration of methylene –$CH_2$–, stretching vibration of C≡N, stretching vibration of C=O, bending vibration of –$CH_2$–, and stretching vibration of the C–N bonds [42–44]. Compared with pure PAN electrospun membrane, the C–N stretching vibration absorption peak of g-$C_3N_4$ located at 1235 $cm^{-1}$

and 1640 $cm^{-1}$, and the characteristic peak of the 3-s-triazine structure located at 814 $cm^{-1}$, appeared in the FTIR spectra of $S_1$, $S_2$, and $S_3$ [45,46]. Therefore, the FTIR results further demonstrated the successful loading of photocatalysts on electrospun membranes. However, due to the low content of $MoS_2$, its characteristic peaks failed to be observed. It should be noted that the intensity and area of the peaks assigned to g-$C_3N_4$ increased in turn from $S_1$ to $S_3$, indicating more photocatalysts were exposed, which was beneficial to improve photocatalytic efficiency.

The chemical status and bonding structures of the PAN-g-$C_3N_4$/$MoS_2$ electrospun membranes were analyzed by X-ray photoelectron spectroscopy (XPS). The full-scale XPS survey spectra revealed the existence of C, N, Mo, and S elements (Figure 4). In addition, the peak differentiation imitating the four elements was studied to further understand the detailed composition (Figure 5). The XPS spectra of C 1s could be deconvoluted into four peaks (Figure 5a), wherein the peaks at 284.5 eV and 286.3 eV were attributed to the $sp^2$ C–C bonds and C-$NH_2$ species of the g-$C_3N_4$ [33]. The peak at 284.7 eV ($sp^2$ C-C) belonged to C 1s of PAN, and the peak at 288.5 eV could be attributed to the carbon in N-C=N [47]. The XPS spectra of N 1 s had three peaks at 398.7 eV, 400.0 eV, and 401.1 eV, respectively (Figure 5b), which could be attributed to the $sp^2$ hybridized nitrogen in C-N=C, tertiary nitrogen N-$(C)_3$ groups, and free amino groups (C-N-H) [33]. Three peaks in the high-resolution XPS spectra of Mo 3d at 225.8 eV, 228.7 eV, and 231.9 eV were further revealed (Figure 5c), belonging to S 2s, Mo $3d_{5/2}$, and Mo $3d_{3/2}$, respectively [47]. It could be confirmed that the Mo element in g-$C_3N_4$/$MoS_2$ was mainly presented in the state of $Mo^{4+}$. Regarding the XPS spectra of S 2p (Figure 5d), two major peaks at 162.4 eV and 163.5 eV could be attributed to S $2p_{3/2}$ and S $2p_{1/2}$, respectively [47]. The XPS results verified that the g-$C_3N_4$/$MoS_2$ was successfully anchored with electrospun PAN membranes.

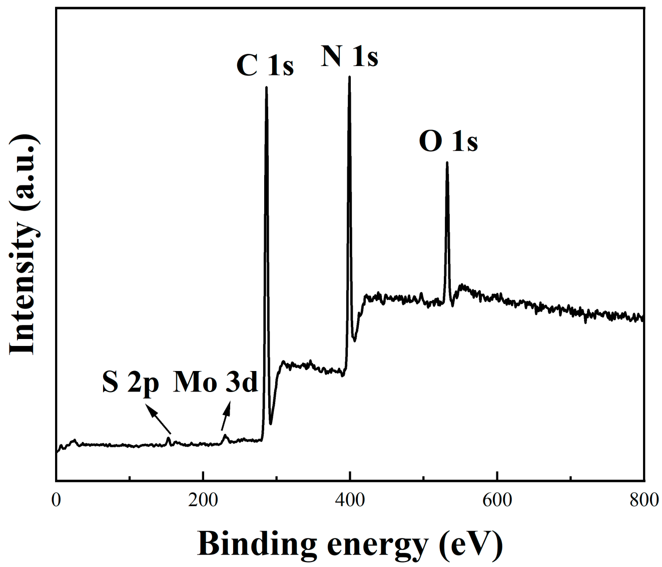


**Figure 4.** The full-scale XPS survey spectra of $S_3$.

Figure 6a illustrates the DRS spectra of g-$C_3N_4$ and g-$C_3N_4$/$MoS_2$ powders. Compared with pure g-$C_3N_4$, the absorption of g-$C_3N_4$/$MoS_2$ has stronger intensity at the UV-visible light range and an obvious red-shift, which meant that the compounding of $MoS_2$ effectively broadens and strengthens the light absorption. The heterojunction constructed between g-$C_3N_4$ and $MoS_2$ changes the optical properties of hybrid materials, promoting the light absorption, and could improve the photocatalytic activity under visible-light irradiation.

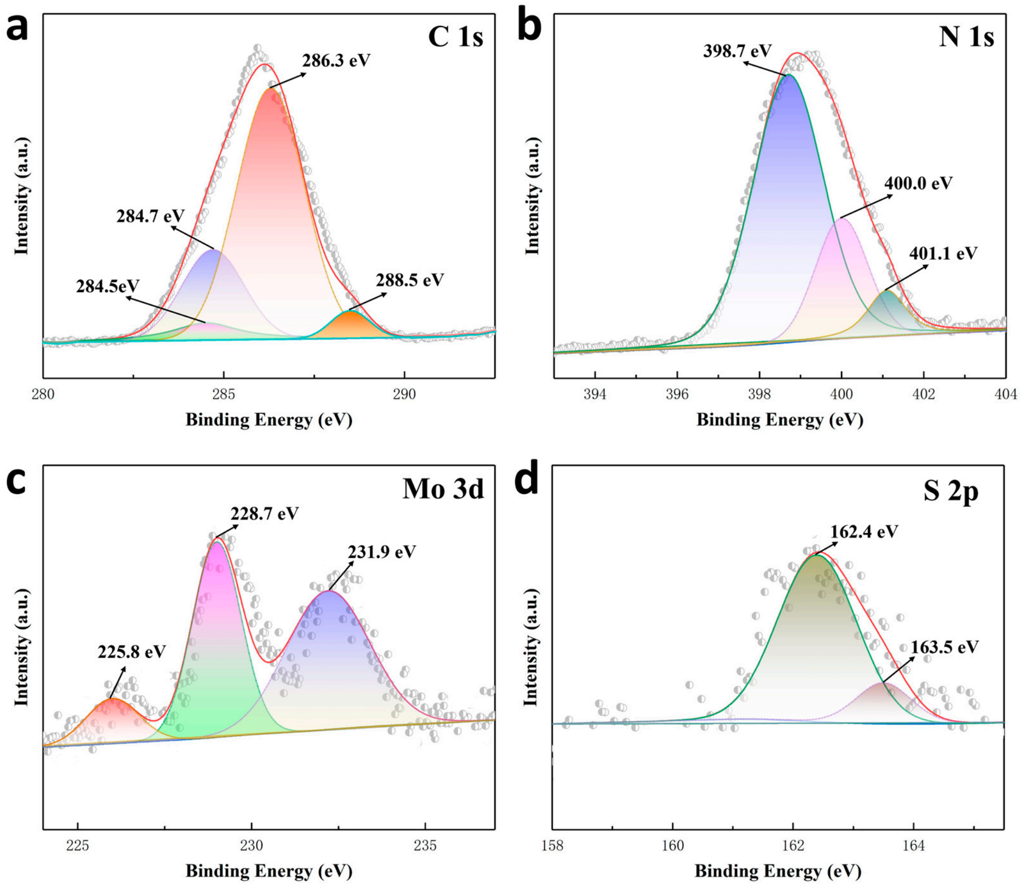


**Figure 5.** The high-resolution XPS spectra of $S_3$: (**a**) C 1s, (**b**) N 1s, (**c**) Mo 3d, and (**d**) S 2p.

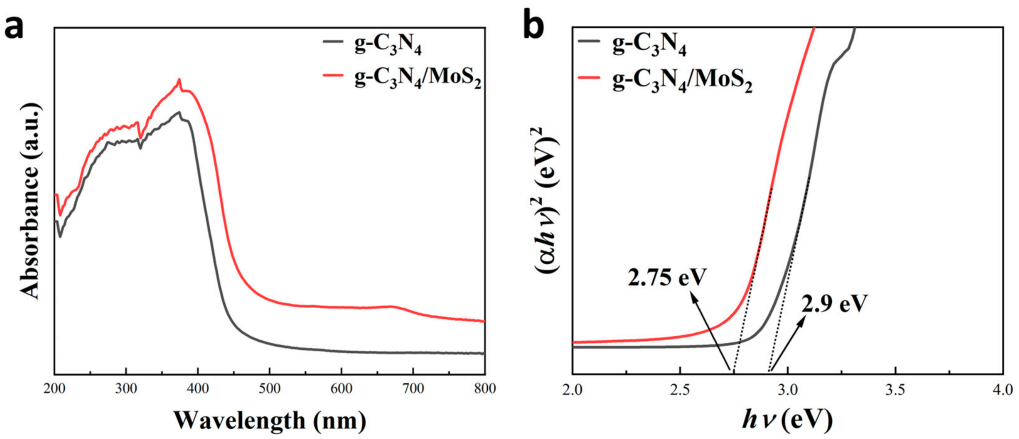


**Figure 6.** (**a**) Diffuse reflectance spectra (DRS) of g-$C_3N_4$ and g-$C_3N_4$/$MoS_2$; (**b**) band gaps estimated respectively by the Kubelka–Munk equation from DRS data.

The results of UV-Vis DRS were used to calculate the band gap energy ($E_g$) of the material through the Kubelka–Munk formula (1):

$$\alpha h\nu = C(h\nu - E_g)^{n/2} \quad (1)$$

where $\alpha$, $h$, $\nu$, and $C$ are the absorption coefficient, Planck constant, optical frequency, and constant, respectively. The value of $n$ is determined by the material properties. Through the Kubelka–Munk formula, the integral band gap of g-$C_3N_4$/$MoS_2$ could be estimated to be 2.75 eV, while that of g-$C_3N_4$ was approximated to be 2.9 eV (Figure 6b). Moreover, g-$C_3N_4$/$MoS_2$ with a narrower band gap should have better photocatalytic performance, according to a previous study [48].

Furthermore, the transient photocurrent (TPC) response of the as-prepared $S_1$, $S_2$, $S_3$, and PAN electrospun membrane was displayed (Figure 7) under the condition of light on and off illuminating by a visible light source (Xe lamp, $\lambda \geq 420$ nm). It is known that the higher the photocurrent intensity, the higher the separation rate of photogenerated carriers. Obviously, PAN electrospun membrane had no response to visible light radiation, whereas the photocurrent density of $S_1$, $S_2$, and $S_3$ significantly increased in turn when the Xe lamp was turned on, indicating that more photogenerated charges were generated, which was mainly due to the increasingly exposed g-$C_3N_4$/$MoS_2$ from $S_1$ to $S_3$. Therefore, the photocatalysts could be completely exposed by optimizing the preparation method to not only enhance the harvest of light but also promote the transfer of photogenerated charges from the inner to the surface, which might improve the photocatalytic efficiency effectively.

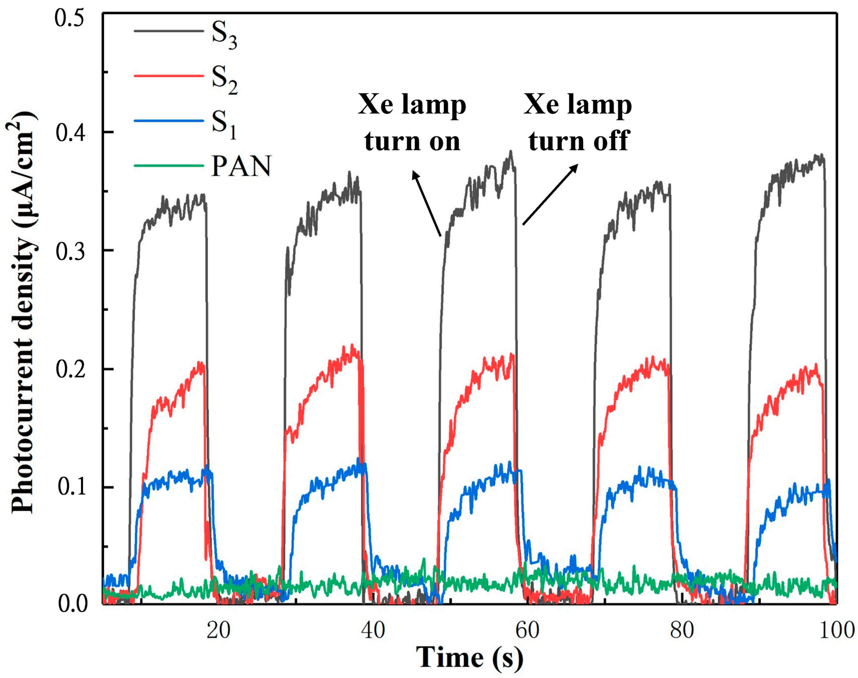


**Figure 7.** Transient photocurrent response curves of $S_1$, $S_2$, $S_3$, and PAN electrospun membrane.

### *2.2. Photocatalysis and Recycling Performance*

Figure 8 shows the photocatalytic degradation of RhB (10 mg/mL) over g-$C_3N_4$/$MoS_2$ with different mass ratios of $MoS_2$ under visible light irradiation. It can be seen that g-$C_3N_4$/$MoS_2$ (1%) had the highest photocatalytic activity, the degradation rate of RhB over which was close to 85% after 90 min. On the other hand, the degradation rate of g-$C_3N_4$ and $MoS_2$ to RhB was about 32% and 20%, respectively, obviously inefficient in comparison with that of the composite photocatalyst. These results confirmed that the strategy of small amount of compounding $MoS_2$ with g-$C_3N_4$ was workable to promote photocatalytic activity, and the best mass ratio of $MoS_2$ in g-$C_3N_4$/$MoS_2$ is 1%.

The photocatalytic performances were comparatively evaluated by photocatalytic degradation of $AFB_1$ aqueous solution under visible light irradiation, and $AFB_1$ aqueous solution without photocatalytic membrane was used as the control group (Figure 9). Before photocatalytic degradation under visible light irradiation, the $AFB_1$ aqueous solution immersed with $S_1$, $S_2$, and $S_3$ was kept in darkness for 30 min to achieve adsorption/desorption equilibrium, and the duration of photocatalytic reaction was 60 min.

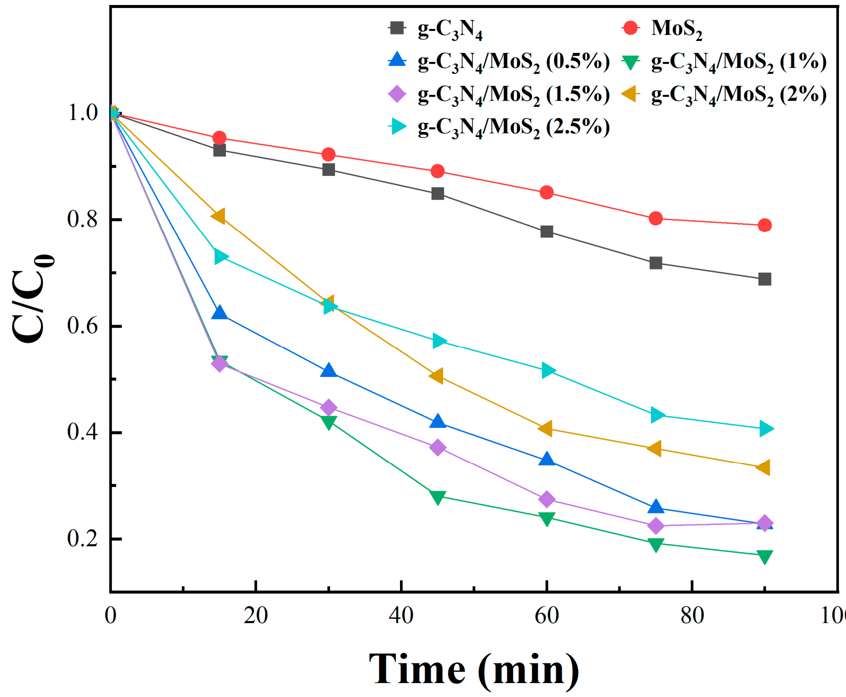


**Figure 8.** Photocatalytic degradation of RhB over g-$C_3N_4/MoS_2$ with different weight ratios of $MoS_2$.

It could be observed that for the blank experiment without a photocatalytic membrane, the concentration of $AFB_1$ was unchanged under visible light irradiation. The photocatalytic activity of $S_1$, $S_2$, and $S_3$ was significantly improved, and the photodegradation efficiency was up to 65.5%, 79.2%, and 96.8% in 60 min, respectively (Figure 9a). These results showed that the degradation of $AFB_1$ was mainly due to a photocatalytic reaction. As we speculated, the efficiency of photocatalytic degradation of $AFB_1$ by $S_1$, $S_2$, and $S_3$ increased in turn. $S_3$ showed greatly higher photocatalytic efficiency with a degradation rate of 31.3% and 17.6% higher than $S_1$ and $S_2$, respectively. This implied that g-$C_3N_4/MoS_2$ anchored on electrospun PAN membranes played an important role in the photocatalytic activity of $AFB_1$ degradation. As the g-$C_3N_4/MoS_2$ anchored on $S_3$ were utterly exposed, the light-harvesting ability was enhanced compared with $S_1$ and $S_2$. Thus, many photogenerated charges were produced in g-$C_3N_4/MoS_2$ and more easily transferred to the surface of the photocatalyst because they were not wrapped by the polymer. More importantly, this fully exposed g-$C_3N_4/MoS_2$ provided more active sites and greatly enhanced the photocatalytic efficiency. The high-performance liquid chromatography (HPLC) chromatogram of $AFB_1$ aqueous solution concentrations with the irradiation time was also demonstrated (Figure 9b).

In a typical photocatalytic process, many factors affect photocatalytic performance. Besides the basic properties (crystal structure, particle size, specific surface area, and surface hydroxyl group) and carrier of the photocatalysts, external environmental factors such as light source, irradiation time, temperature, pH value, and initial concentration of reactants also make a certain sense [49]. In this study, the influence of pH values and initial concentrations of $AFB_1$ on photocatalytic efficiency was estimated, which were two variable factors in practical application.

$S_3$ was used to study the photocatalytic efficiency at pH values of 3, 5, 7, and 9, whereas the concentrations of $AFB_1$ were kept constant (Figure 9c). It was observed that the degradation of $AFB_1$ was suppressed in an acidic aqueous solution. With the increase in pH value, the photocatalytic degradation rates of $AFB_1$ increased accordingly. In the neutral solution with a pH value of 7, nearly 17% of $AFB_1$ was adsorbed after 30 min. However, in the acidic solution with pH values of 3 and 5, only 8% and 13% of $AFB_1$ were adsorbed, indicating that the high photocatalytic degradation efficiency might come from high adsorption. The photocatalytic membranes and AFB1 (pH = 5) were positively charged in an acidic solution [26]. The absorption of AFB1 on the active site was low due to the repulsive force between the photocatalytic membranes and AFB1 [26,38]. Subsequently, the photocatalytic efficiency was weakened.

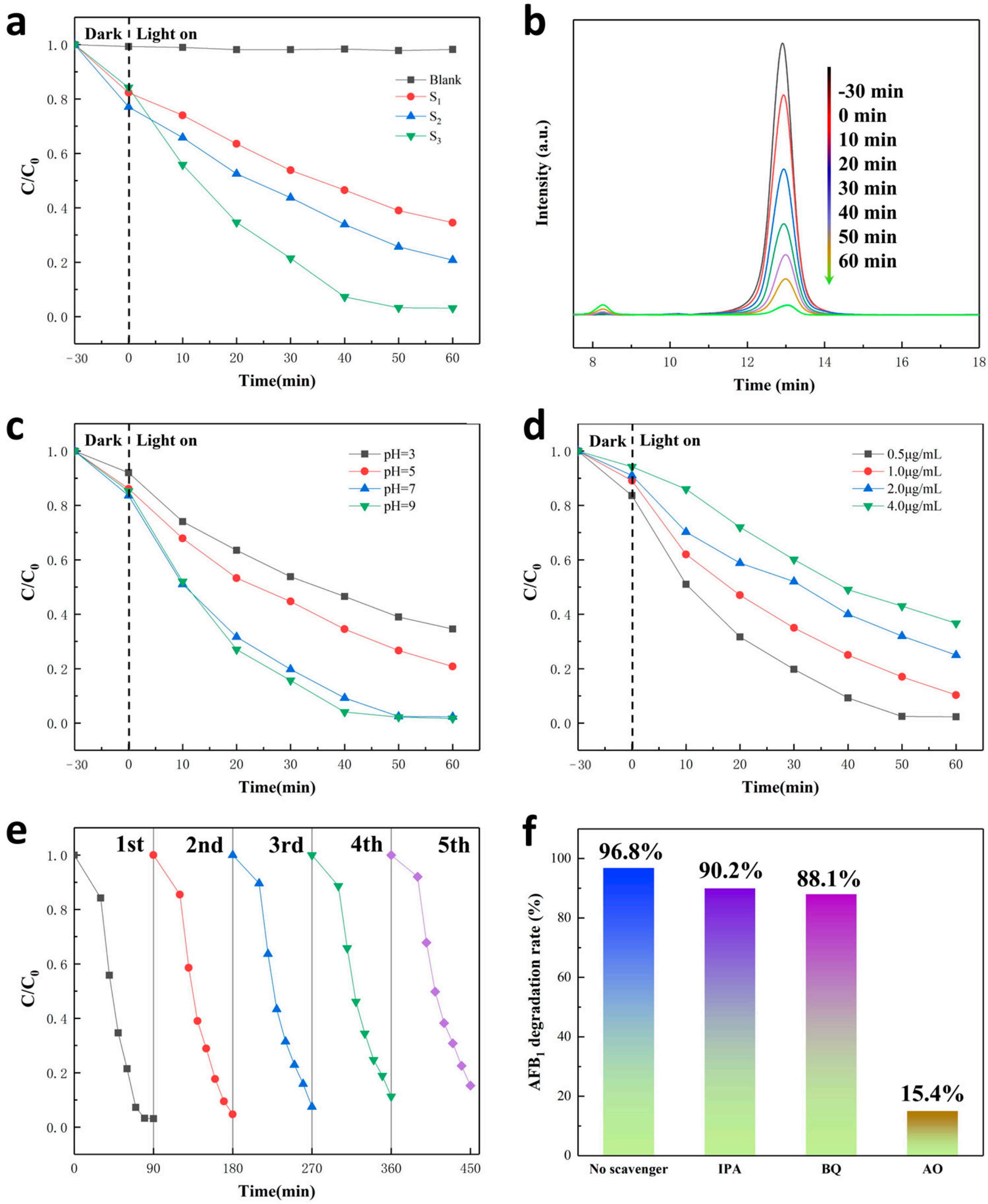


**Figure 9.** (**a**) Photocatalytic degradation efficiencies of $AFB_1$ with as-prepared $S_1$, $S_2$, and $S_3$ under visible light irradiation. (**b**) HPLC chromatogram of $AFB_1$ photocatalytic degradation with $S_3$ under visible light irradiation at different times. (**c**) The photocatalytic activity of $S_3$ for degradation of $AFB_1$ at different pH values. (**d**) The photocatalytic activity of $S_3$ for degradation of $AFB_1$ with different initial concentrations. (**e**) The photocatalytic activity of $S_3$ for degradation of $AFB_1$ for five cycles. (**f**) Photocatalytic activities of $S_3$ for the degradation of $AFB_1$ in the presence of different scavengers.

For the same reason, in an alkaline solution with a pH value of 9, there was a similar repulsive force between the photocatalytic membranes and $AFB_1$. However, the photocatalytic degradation efficiency was not decreased but instead slightly increased. The reason might be that $AFB_1$ was unstable in the alkaline environment [50]. To investigate the effect of the $AFB_1$ initial concentration on the photocatalytic degradation efficiency, $S_3$ was soaked in different initial concentrations of $AFB_1$ (0.5–4 μg/mL, i.e., 500–4000 PPb) with a pH value of 7 (Figure 9d). It was observed that the photocatalytic degradation efficiency was inversely related to $AFB_1$ initial concentration. The $AFB_1$ degradation efficiencies were 97.5% and 63.3% at initial concentrations of 500 and 4000 PPb, respectively. This could be assigned to a constant number of active sites on the photocatalytic membrane. With the increase of initial concentrations and the proceeding of the photocatalytic reaction, competitive adsorption of $AFB_1$ and its intermediates on the photocatalytic membranes would be aggravated, subsequently affecting the harvest of light and forming a barrier against photoexcitation in g-$C_3N_4$/$MoS_2$ [28,51].

For the practical application of the photocatalytic membranes, five consecutive photocatalytic experiments were carried out using $S_3$ under the same experimental conditions with proper washing and drying after each cycle (Figure 9e). The reproducibility results of $AFB_1$ degradation by $S_3$ showed that although the degradation pace decreased slightly after each photocatalytic degradation test, the degradation rate reached more than 85% overall. The slight decrease in degradation rate might be due to the contaminant of reused samples during the recovery step by the intermediate products produced in the photocatalytic degradation of $AFB_1$. The recyclability of the photocatalytic membranes verified the possibility of practical application and a better economic benefit.

To better understand the mechanism of photocatalytic degradation of $AFB_1$ by the PAN-g-$C_3N_4$/$MoS_2$ electrospun membranes, the active species trapping experiments were carried out using $S_3$ under the same conditions described above (Figure 9f). Isopropanol (IPA), 1,4-benzoquinone (BQ), and ammonium oxalate (AO) were employed as the scavengers for hydroxyl radicals (•OH), super-oxide anion radicals ($•O_2^-$), and photogenerated holes ($h^+$), respectively [52]. After 60 min of visible light irradiation, the degradation rate of $AFB_1$ without a sacrificial agent was 96.8%, and for others with scavengers IPA, BQ, and AO, the degradation rate was 90.2%, 88.1%, and 15.4%, respectively. Therefore, it could be confirmed that $h^+$ was the main active specie in the reaction process.

### *2.3. Mechanism for Enhanced Degradation Performance*

Based on the previous results, the possible photocatalytic mechanism of $AFB_1$ degradation by the PAN-g-$C_3N_4$/$MoS_2$ electrospun membranes was proposed (Figure 10). It could be regarded that g-$C_3N_4$/$MoS_2$ anchored on PAN electrospun membranes was simultaneously excited under visible light irradiation and produced photo-induced electrons and holes. According to previous studies and band gap values estimated by the Kubelka–Munk formula, the conduction band of g-$C_3N_4$ (−1.22 eV) is higher than that of $MoS_2$ (−0.12 eV), and the valence band of $MoS_2$ (1.78 eV) is lower than that of g-$C_3N_4$ (1.68 eV) [53]. The photo-induced electrons produced in g-$C_3N_4$ can be easily transferred to the conduction band of $MoS_2$ through the interface, and the photo-induced holes produced in $MoS_2$ transfer to the valence band of g-$C_3N_4$ in a similar manner. As a result, the photo-induced electrons are gathered in the conduction band of $MoS_2$, and the photo-induced holes are gathered in the valence band of g-$C_3N_4$, which leads to photo-induced electrons and holes to separate effectively. Therefore, the probability of photo-induced electron-hole recombination is hindered, and the photocatalytic efficiency is improved accordingly. However, the conduction band potential of $MoS_2$ is more positive than the potential of $E(O_2/•O_2^-)$ (−0.12 V > −0.33 V) [54]; the electrons on the conduction band of $MoS_2$ cannot react with $O_2$ to generate $•O_2^-$. For the same reason, the holes on the valence band of g-$C_3N_4$ cannot generate •OH, as the valence band of g-$C_3N_4$ is more negative than the potential of $E(OH^-/•OH)$ or $E(H_2O/•OH)$ (1.56 V < 1.99 or 2.4 V) [55]. Thereby, rich holes in the valence band of g-$C_3N_4$ act as the main reactive species to oxidize $AFB_1$ directly, consistent with the results of active species trapping experiments. The reaction formulas are as follows:

$$g\text{-}C_3N_4/MoS_2 + h\nu \rightarrow e^-(CB) + h^+(VB) \quad (2)$$

$$AFB_1 + h^+ \rightarrow CO_2 + H_2O + \text{intermediate products} \quad (3)$$

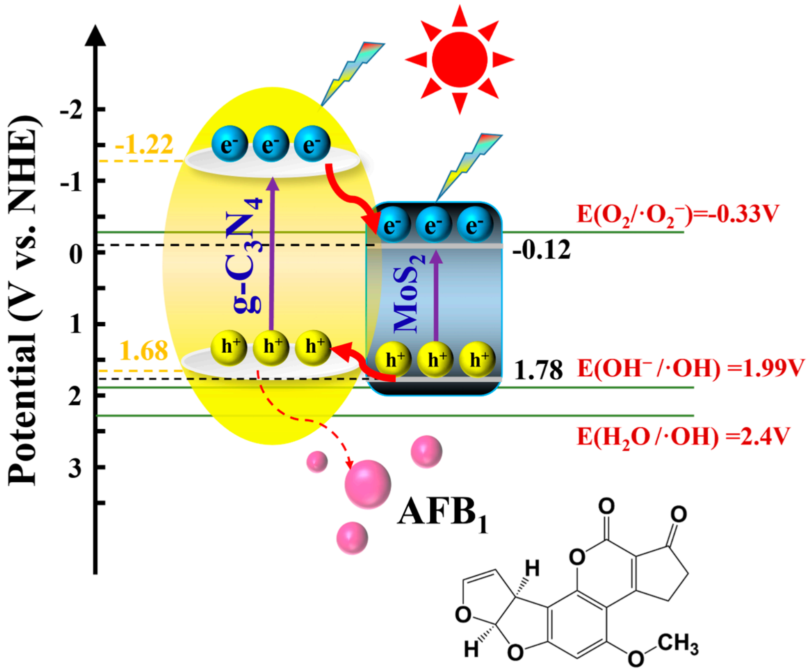


**Figure 10.** The photocatalytic mechanism of PAN-g-$C_3N_4/MoS_2$ electrospun membranes for degradation of $AFB_1$ [53].

## 3. Conclusions

Three kinds of flexible electrospun membranes anchored with g-$C_3N_4/MoS_2$ composites were synthesized via uniaxial or coaxial electrospinning techniques. Due to more g-$C_3N_4/MoS_2$ photocatalysts being exposed and more active sites being produced, the photocatalytic efficiency of $S_1$, $S_2$, and $S_3$ increased gradually. The degradation efficiency of $AFB_1$ solution with a concentration of 500 PPb (50 mL) was up to 97% in 60 min under visible light irradiation with 0.025 g $S_3$. The mechanism of photocatalytic membranes degradation of $AFB_1$ in the photocatalytic process was proposed based on active species trapping experiments, and the reusability and stable activity were confirmed after five cycles of photocatalytic degradation experiments. Thus, the PAN-g-$C_3N_4/MoS_2$ electrospun membranes were proved as high photocatalytic activity, easy separation, good reusability, and potential practical application in the foodstuff for the degradation of $AFB_1$.

## 4. Materials and Methods

### *4.1. Materials and Reagents*

$AFB_1$ was purchased from Beijing Puhuashi Technology Development Co., Ltd. (Beijing, China), and dissolved to a certain concentration with deionized water. Melamine (≥99.0% purity), sodium molybdate (≥99.0% purity), thioacetamide (≥99.0% purity), N,N-dimethylformamide (DMF, AR, 99.5%), N-methyl pyrrolidone (NMP, ≥99.0%), anhydrous ethanol (AR, 99.5%), glacial acetic acid (for HPLC, ≥99.9%), trifluoroacetate (for HPLC, ≥99.5%), methanol (for HPLC, ≥99.9%), and acetonitrile (for HPLC, ≥99.9%) were purchased from Macklin Biochemical Co., Ltd. PAN (Mw ≈ 120,000) and PEO (Mw ≈ 200,000) were obtained from Sigma-Aldrich Co., Ltd. All reagents were used without any further purification. The deionized water used in this study was purified by a Millipore system.

*4.2. Preparation of g-$C_3N_4$/$MoS_2$*

As shown in Scheme 1, the g-$C_3N_4$ powders were prepared by calcining melamine at 550 °C for 3 h (5 °C/min). The $MoS_2$ powders were prepared by hydrothermal process. In a typical procedure, 20 mg sodium molybdate and 25 mg thioacetamide were dissolved in 30 mL deionized water under magnetic stirring for 20 min. Then, the above solution was poured into a stainless-steel autoclave, and the reaction temperature was controlled at 200 °C by the oven for 24 h. Following several times washing with deionized water and ethanol, the resultants dried at 60 °C for 10 h under vacuum were $MoS_2$ powders.

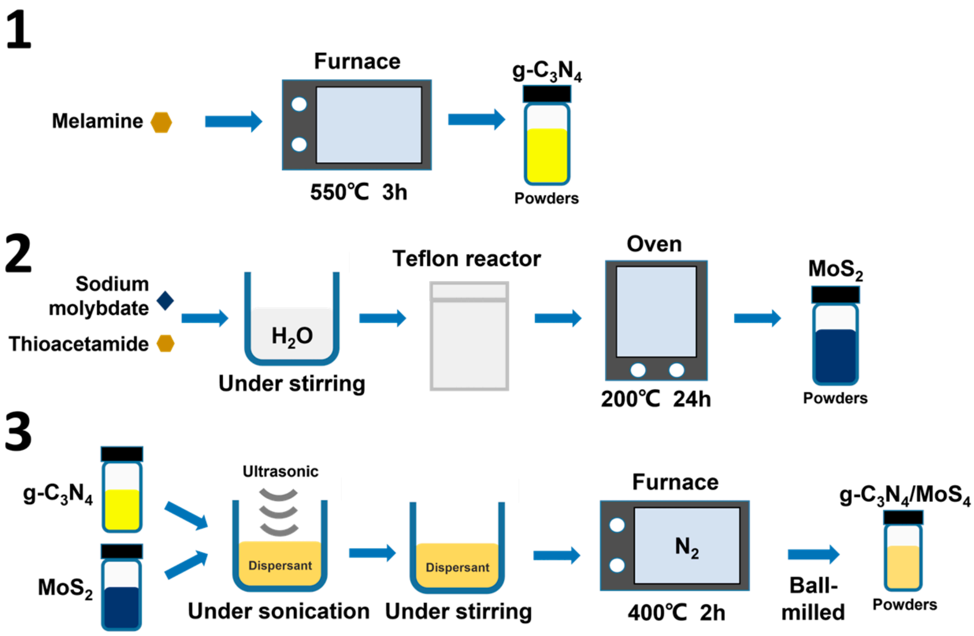


**Scheme 1.** The schematic illustration of the fabrication of g-$C_3N_4$, $MoS_2$, and g-$C_3N_4$/$MoS_2$.

The g-$C_3N_4$/$MoS_2$ composites were fabricated by low-temperature calcination, and the mass ratio of $MoS_2$ in g-$C_3N_4$/$MoS_2$ was determined as 1% in this study. Firstly, 198 mg g-$C_3N_4$ and 2 mg $MoS_2$ powders were dispersed in NMP and absolute ethanol, respectively, and ultrasonicated for 60 min. The two solutions were then mixed and stirred for 12 h, and the precipitates obtained after centrifugation were washed with deionized water and ethanol several times and dried at 80 °C for 10 h under vacuum. Secondly, the precipitates were ground to powders and followed by annealing at 400 °C for 2 h with a ramping speed of 5 °C/min in a nitrogen atmosphere. Finally, the g-$C_3N_4$/$MoS_2$ composites were ball-milled for 3 h after cooling to room temperature for future use. According to the above scheme, the g-$C_3N_4$/$MoS_2$ composites with different $MoS_2$ mass contents 0.5%, 1.5%, 2%, and 2.5% were prepared by changing the amount of $MoS_2$ added.

*4.3. Preparation of PAN-g-C3N4/MoS2 Electrospun Membranes*

Three kinds of PAN-g-$C_3N_4$/$MoS_2$ electrospun membranes were fabricated by electrospinning (Scheme 2). For the first one, a certain amount of g-$C_3N_4$/$MoS_2$ composites was added into DMF and ultrasonicated for 1 h to disperse the photocatalysts. Subsequently, PAN was added and stirred for 2 h to obtain a yellow-grey solution. The concentration of PAN in DMF was 12 *w*/*v*%, and the contents of g-$C_3N_4$/$MoS_2$ composites to DMF was 3 *w*/*v*%. The prepared solution was then injected into a plastic syringe with a metal needle driven by a syringe pump at a flow rate of 1.5 mL/h for electrospinning. The applied voltage was 10 kV, and the distance from the metallic needle to the aluminum foil surface was 15 cm. After electrospinning, the electrospun membranes were dried at 60 °C under vacuum for 12 h, recorded as $S_1$. The second one was prepared according to $S_1$ with some modifications. Typically, the polymer added into DMF was changed to

PAN/PEO (PAN: PEO = 2:1, wt%), while keeping the total concentration of the polymer constant with $S_1$ (12 *w*/*v*%). After drying at 60 °C under vacuum for 12 h, the electrospun membranes were immersed in deionized water, sonicated in a water bath for 1 h, and placed at 60 °C for 24 h to fully wash out PEO. The washed electrospun membranes were dried at 60 °C under vacuum for 12 h, recorded as $S_2$. The third one was prepared by a simple coaxial electrospinning technique. The core solution with concentration PAN 12 *w*/*v*% was prepared similarly to $S_1$ without adding g-$C_3N_4$/$MoS_2$ composites. The sheath solution was prepared with PEO, g-$C_3N_4$/$MoS_2$, and DMF similar to $S_1$. The concentration of PEO in DMF was set to 7 *w*/*v*%, and the contents of g-$C_3N_4$/$MoS_2$ composites to DMF were 3 *w*/*v*%. The core and sheath solution was pumped out at rates of 1.5 mL/h using two syringe pumps, and the applied voltage and the distance from the metallic needle to the aluminum foil surface were set to be the same as both $S_1$ and $S_2$. The resultant electrospun membranes were washed with deionized water and dried at 60 °C under vacuum for 12 h, recorded as $S_3$.

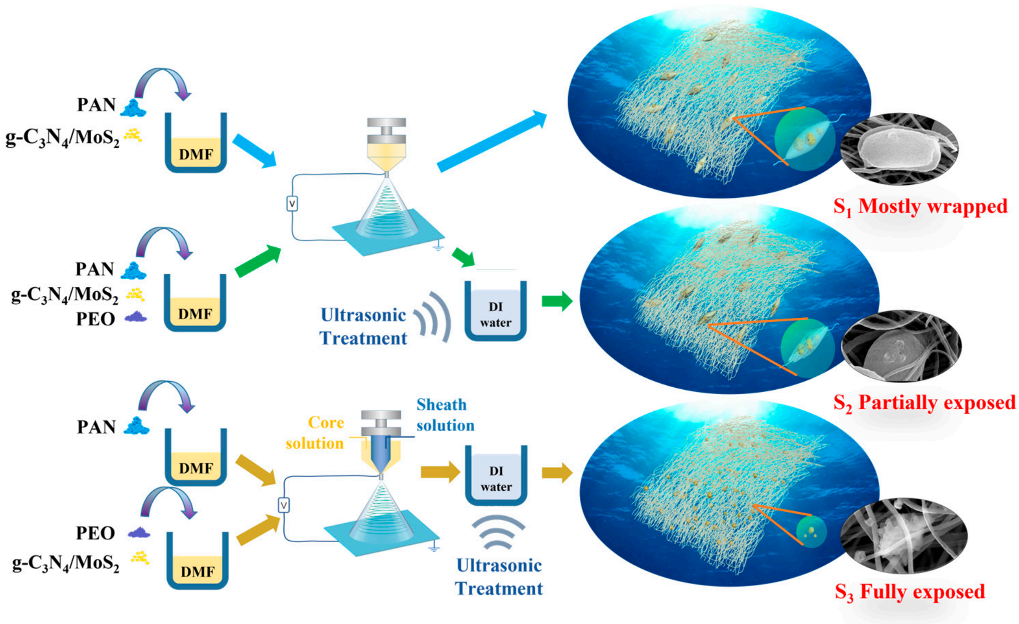


**Scheme 2.** The schematic illustration of the fabrication of $S_1$, $S_2$, and $S_3$.

### 4.4. Characterization of PAN-g-$C_3N_4$/$MoS_2$ Electrospun Membranes

The morphologies of the PAN-g-$C_3N_4$/$MoS_2$ electrospun membranes were observed by SEM (ZEISS Sigma, Aalen, Germany), and the microstructure of g-$C_3N_4$/$MoS_2$ composites were observed by TEM (JEM-2100F). XRD patterns was obtained with an X-ray diffractometer (MiniFlex 600, Tokyo, Japan) at a scanning speed of 2°/min. FTIR spectra were analyzed on a Vector-22 spectrometer. High-resolution XPS spectra were analyzed by an X-ray photoelectron spectrometer. DRS was detected by a UV/VIS spectrophotometer (Shimadzu UV-3600 Plus, Tokyo, Japan). TPC curves were tested on a three-electrode electrochemical workstation (CHI600E, Beijing, China) with PAN-g-$C_3N_4$/$MoS_2$ electrospun membranes/glassy as the working electrode, Ag/AgCl as the reference electrode, and platinum wire as the counter electrode, respectively. The electrolyte was 0.1 M $Na_2SO_4$ aqueous solution.

### 4.5. Photocatalytic Degradation Experiment

The degradation of $AFB_1$ was evaluated in an aqueous medium under visible light irradiation by a 300 W xenon lamp with a 400 nm cut-off filter. Samples from electrospun membranes were cut into a circular shape (2 cm in diameter and approximately 0.025 g in weight) and fixed on a bracket, immersed in 50 mL of $AFB_1$ aqueous solution (500 PPb). Then, it was placed in the dark for 30 min to establish the adsorption/desorption equilibrium before light irradiation. The distance between the xenon lamp and the aqueous surface was 10 cm. In the progress of the photocatalytic degradation, 0.5 mL of the $AFB_1$ aqueous solution was collected every 10 min and then added 0.25 mL glacial acetic acid and 0.25 mL trifluoroacetic acid. The mixed solution was put in a water bath at 70 °C for 40 min to enhance the fluorescence emission intensity of $AFB_1$ when detected by HPLC. The concentration of the $AFB_1$ was analyzed by the HPLC on Waters-600 equipped with a UV/Vis detector (emission wavelength at 365 nm) and C-18 Phenomenex reverse phase column (250 × 4.6 mm i.d., 5 μm) at a flow rate of 1 mL/min with an isocratic system composed of water: methanol: acetonitrile (70:20:10). Different factors were also analyzed, such as pH values (4–10) and initial concentration of $AFB_1$. The $AFB_1$ solution without electrospun membranes upon irradiation was also monitored in order to quantify the photocatalytic degradation of $AFB_1$. The stability of the electrospun membranes was evaluated over 5 continuous cycle experiments under visible light irradiation. After each cycle, the electrospun membranes were rinsed with deionized water for continued use.

To explore the mechanism of degradation of $AFB_1$ by the electrospun membranes, active species trapping experiments were carried out by using the addition of IPA (1 mM), AO (1 mM), and BQ (1 mM) to capture hydroxyl radicals (•OH), photogenerated holes ($h^+$), and super-oxide anion radicals (•$O_2^-$), respectively.

**Supplementary Materials:** The following supporting information can be downloaded at: https://www.mdpi.com/article/10.3390/toxins15020133/s1, Figure S1: Photocatalytic degradation of RhB with different weight ratios of g-C3N4 and MoS2.

**Author Contributions:** Conceptualization, D.Z. and C.S.; methodology, R.S. and L.Y.; validation, R.S. and L.Y.; formal analysis, R.S. and L.Y.; investigation, R.S.; resources, D.Z. and G.L.; data curation, R.S.; writing—original draft preparation, R.S.; writing—review and editing, L.Y., D.Z., D.Y. and Z.L.; visualization, R.S.; supervision, D.Z., D.Y. and H.L.; project administration, D.Z. and S.Z. All authors have read and agreed to the published version of the manuscript.

**Funding:** This research was funded by the National Natural Science Foundation of China (62275160).

**Institutional Review Board Statement:** Not applicable.

**Informed Consent Statement:** Not applicable.

**Data Availability Statement:** Raw data are available on request.

**Acknowledgments:** The authors give special thanks to Dengguang Yu from University of Shanghai for Science and Technology. The authors also thank Ding Wang at the University of Shanghai for Science and Technology for providing the SEM and TEM measurements used in this study.

**Conflicts of Interest:** The authors declare no conflict of interest. The funders had no role in the design of the study; in the collection, analysis, or interpretation of data; in the writing of the manuscript; or in the decision to publish the results.

## References

1. Wild, C.P.; Turner, P.C. The toxicology of aflatoxins as a basis for public health decisions. *Mutagenesis* **2002**, *17*, 471–481. [CrossRef] [PubMed]
2. Wu, F.; Groopman, J.D.; Pestka, J.J. Public health impacts of foodborne mycotoxins. *Annu. Rev. Food Sci. Technol.* **2014**, *52014*, 351–372. [CrossRef] [PubMed]
3. Kumar, P.; Mahato, D.K.; KamLe, M.; Mohanta, T.K.; Kang, S.G. Aflatoxins: A global concern for food safety, human health and their management. *Front. Microbiol.* **2017**, *7*, 2170. [CrossRef] [PubMed]
4. Sherif, O.S.; Salama, E.E.; Abdel-Wahhab, M.A. Mycotoxins and child health: The need for health risk assessment. *Int. J. Hyg. Environ. Health* **2009**, *212*, 347–368.
5. Wild, C.P.; Gong, Y.Y. Mycotoxins and human disease: A largely ignored global health issue. *Carcinogenesis* **2010**, *31*, 71–82. [CrossRef]
6. Fan, T.; Xie, Y.; Ma, W. Research progress on the protection and detoxification of phytochemicals against aflatoxin $B_1$-induced liver toxicity. *Toxicon* **2021**, *195*, 58–68. [CrossRef]
7. IARC. Some naturally occurring substances: Food items and constituents, heterocyclic aromatic amines and mycotoxins. *IARC Monogr. Eval. Carcinog. Risks Hum.* **1993**, *56*, 489–521.

8. Liu, Y.; Wu, F. Global burden of aflatoxin-induced hepatocellular carcinoma: A risk assessment. *Environ. Health Perspect.* **2010**, *118*, 818–824. [CrossRef]
9. El-Serag, H.B. Epidemiology of viral hepatitis and hepatocellular carcinoma. *Gastroenterology* **2012**, *143*, 269. [CrossRef]
10. Joubert, O. Chronic and acute toxicities of aflatoxins: Mechanisms of action. *Environ. Risques Sante* **2020**, *19*, 296–297.
11. Streit, E.; Schatzmayr, G.; Tassis, P.; Tzika, E.; Marin, D.; Taranu, I.; Tabuc, C.; Nicolau, A.; Aprodu, I.; Puel, O.; et al. Current situation of mycotoxin contamination and co-occurrence in animal feed-focus on europe. *Toxins* **2012**, *4*, 788–809. [CrossRef]
12. Xiong, J.L.; Wang, Y.M.; Zhou, H.L.; Liu, J.X. Effects of dietary adsorbent on milk aflatoxin $m_1$ content and the health of lactating dairy cows exposed to long-term aflatoxin $B_1$ challenge. *J. Dairy Sci.* **2018**, *101*, 8944–8953. [CrossRef]
13. De Jesus Nava-Ramirez, M.; Salazar, A.M.; Sordo, M.; Lopez-Coello, C.; Tellez-Isaias, G.; Mendez-Albores, A.; Vazquez-Duran, A. Ability of low contents of biosorbents to bind the food carcinogen aflatoxin $B_1$ in vitro. *Food Chem.* **2021**, *345*, 128863. [CrossRef]
14. Li, S.; Luo, J.; Fan, J.; Chen, X.; Wan, Y. Aflatoxin $B_1$ removal by multifunctional membrane based on polydopamine intermediate layer. *Sep. Purif. Technol.* **2018**, *199*, 311–319. [CrossRef]
15. Isikber, A.A.; Athanassiou, C.G. The use of ozone gas for the control of insects and micro-organisms in stored products. *J. Stored Prod. Res.* **2015**, *64*, 139–145. [CrossRef]
16. Yu, Y.; Shi, J.; Xie, B.; He, Y.; Qin, Y.; Wang, D.; Shi, H.; Ke, Y.; Sun, Q. Detoxification of aflatoxin $B_1$ in corn by chlorine dioxide gas. *Food Chem.* **2020**, *328*, 127121. [CrossRef]
17. Yousefi, M.; Shariatifar, N.; Ebrahimi, M.T.; Mortazavian, A.M.; Mohammadi, A.; Khorshidian, N.; Arab, M.; Hosseini, H. In vitro removal of polycyclic aromatic hydrocarbons by lactic acid bacteria. *J. Appl. Microbiol.* **2019**, *126*, 954–964. [CrossRef]
18. Guan, Y.; Chen, J.; Nepovimova, E.; Long, M.; Wu, W.; Kuca, K. Aflatoxin detoxification using microorganisms and enzymes. *Toxins* **2021**, *13*, 46. [CrossRef]
19. Fujishima, A.; Honda, K. Electrochemical photolysis of water at a semiconductor electrode. *Nature* **1972**, *238*, 37–38. [CrossRef]
20. Bai, X.; Sun, C.; Liu, D.; Luo, X.; Li, D.; Wang, J.; Wang, N.; Chang, X.; Zong, R.; Zhu, Y. Photocatalytic degradation of deoxynivalenol using graphene/ZnO hybrids in aqueous suspension. *Appl. Catal. B* **2017**, *204*, 11–20. [CrossRef]
21. Mboula, V.M.; Hequet, V.; Gru, Y.; Colin, R.; Andres, Y. Assessment of the efficiency of photocatalysis on tetracycline biodegradation. *J. Hazard. Mater.* **2012**, *209*, 355–364. [CrossRef] [PubMed]
22. Mao, J.; Li, P.; Wang, J.; Wang, H.; Zhang, Q.; Zhang, L.; Li, H.; Zhang, W.; Peng, T. Insights into photocatalytic inactivation mechanism of the hypertoxic site in aflatoxin $B_1$ over clew-like $WO_3$ decorated with CdS nanoparticles. *Appl. Catal. B* **2019**, *248*, 477–486. [CrossRef]
23. Mao, J.; Zhang, L.; Wang, H.; Zhang, Q.; Zhang, W.; Li, P. Facile fabrication of nanosized graphitic carbon nitride sheets with efficient charge separation for mitigation of toxic pollutant. *Chem. Eng. J.* **2018**, *342*, 30–40. [CrossRef]
24. Yao, L.; Sun, C.; Lin, H.; Li, G.; Lian, Z.; Song, R.; Zhuang, S.; Zhang, D. Electrospun Bi-decorated $Bi_xTi_yO_z/TiO_2$ flexible carbon nanofibers and their applications on degradating of organic pollutants under solar radiation. *J. Mater. Sci. Technol.* **2022**. [CrossRef]
25. Mao, J.; Zhang, Q.; Li, P.; Zhang, L.; Zhang, W. Geometric architecture design of ternary composites based on dispersive $WO_3$ nanowires for enhanced visible-light-driven activity of refractory pollutant degradation. *Chem. Eng. J.* **2018**, *334*, 2568–2578. [CrossRef]
26. Sun, S.; Zhao, R.; Xie, Y.; Liu, Y. Photocatalytic degradation of aflatoxin $B_1$ by activated carbon supported $TiO_2$ catalyst. *Food Control* **2019**, *100*, 183–188. [CrossRef]
27. Zhang, J.; Gao, X.; Guo, W.; Wu, Z.; Yin, Y.; Li, Z. Enhanced photocatalytic activity of $TiO_2$/UiO-67 under visible-light for aflatoxin $B_1$ degradation. *RSC Adv.* **2022**, *12*, 6676–6682. [CrossRef]
28. Raesi, S.; Mohammadi, R.; Khammar, Z.; Paimard, G.; Abdalbeygi, S.; Sarlak, Z.; Rouhi, M. Photocatalytic detoxification of aflatoxin $B_1$ in an aqueous solution and soymilk using nano metal oxides under UV light: Kinetic and isotherm models. *LWT-Food Sci. Technol.* **2022**, *154*, 112638. [CrossRef]
29. Sun, D.; Mao, J.; Cheng, L.; Yang, X.; Li, H.; Zhang, L.; Zhang, W.; Zhang, Q.; Li, P. Magnetic g-$C_3N_4/NiFe_2O_4$ composite with enhanced activity on photocatalytic disinfection of aspergillus flavus. *Chem. Eng. J.* **2021**, *418*, 129417. [CrossRef]
30. Wang, H.; Mao, J.; Zhang, Z.; Zhang, Q.; Zhang, L.; Li, P. Photocatalytic degradation of deoxynivalenol over dendritic-like $\alpha$-$Fe_2O_3$ under visible light irradiation. *Toxins* **2019**, *11*, 105. [CrossRef]
31. Li, G.; Lian, Z.; Wang, W.; Zhang, D.; Li, H. Nanotube-confinement induced size-controllable g-$C_3N_4$ quantum dots modified single-crystalline $TiO_2$ nanotube arrays for stable synergetic photoelectrocatalysis. *Nano Energy* **2016**, *19*, 446–454. [CrossRef]
32. Song, J.; Wang, X.; Yan, J.; Yu, J.; Sun, G.; Ding, B. Soft Zr-doped $TiO_2$ nanofibrous membranes with enhanced photocatalytic activity for water purification. *Sci. Rep.* **2017**, *7*, 1636. [CrossRef]
33. Zheng, X.; Liu, Y.; Liu, X.; Li, Q.; Zheng, Y. A novel PVDF-$TiO_2$@g-$C_3N_4$ composite electrospun fiber for efficient photocatalytic degradation of tetracycline under visible light irradiation. *Ecotoxicol. Environ. Saf.* **2021**, *210*, 111866. [CrossRef]
34. Thi Kim Anh, N.; Thanh-Truc, P.; Huy, N.-P.; Shin, E.W. The effect of graphitic carbon nitride precursors on the photocatalytic dye degradation of water-dispersible graphitic carbon nitride photocatalysts. *Appl. Surf. Sci.* **2021**, *537*, 148027.
35. Jiang, L.; Yuan, X.; Pan, Y.; Liang, J.; Zeng, G.; Wu, Z.; Wang, H. Doping of graphitic carbon nitride for photocatalysis: A reveiw. *Appl. Catal. B* **2017**, *217*, 388–406. [CrossRef]
36. Wu, M.; Li, L.; Liu, N.; Wang, D.; Xue, Y.; Tang, L. Molybdenum disulfide ($MoS_2$) as a co-catalyst for photocatalytic degradation of organic contaminants: A review. *Process Saf. Environ. Prot.* **2018**, *118*, 40–58. [CrossRef]

37. Li, J.; Wu, W.; Li, Y.; Zhang, H.; Xu, X.; Jiang, Y.; Lin, K. In situ synthesized rodlike $MoS_2$ as a cocatalyst for enhanced photocatalytic hydrogen evolution by graphitic carbon nitride without a noble metal. *ACS Appl. Energy Mater.* **2021**, *4*, 11836–11843. [CrossRef]
38. Marinho, B.A.; de Souza, S.M.A.G.U.; de Souza, A.A.U.; Hotza, D. Electrospun $TiO_2$ nanofibers for water and wastewater treatment: A review. *J. Mater. Sci.* **2021**, *56*, 5428–5448. [CrossRef]
39. Zhao, Z.; Luo, S.; Ma, P.; Luo, Y.; Wu, W.; Long, Y.; Ma, J. In situ synthesis of $MoS_2$ on $C_3N_4$ to form $MoS_2/C_3N_4$ with interfacial Mo-N coordination for electrocatalytic reduction of $N_2$ to $NH_3$. *ACS Sustain. Chem. Eng.* **2020**, *8*, 8814–8822. [CrossRef]
40. Zhang, Z.-G.; Liu, H.; Wang, X.-X.; Zhang, J.; Yu, M.; Ramakrishna, S.; Long, Y.-Z. One-step low temperature hydrothermal synthesis of flexible $TiO_2$/PVDF@$MoS_2$ core-shell heterostructured fibers for visible-light-driven photocatalysis and self-cleaning. *Nanomaterials* **2019**, *9*, 431. [CrossRef]
41. D'Elia, A.; Cibin, G.; Robbins, P.E.; Maggi, V.; Marcelli, A. Design and characterization of a mapping device optimized to collect XRD patterns from highly inhomogeneous and low density powder samples. *Nucl. Instrum. Methods Phys. Res. Sect. B* **2017**, *411*, 22–28. [CrossRef]
42. Xie, R.; Zhang, L.; Liu, H.; Xu, H.; Zhong, Y.; Sui, X.; Mao, Z. Construction of CQDs-$Bi_{20}TiO_{32}$/PAN electrospun fiber membranes and their photocatalytic activity for isoproturon degradation under visible light. *Mater. Res. Bull.* **2017**, *94*, 7–14. [CrossRef]
43. Liang, H.; Bai, J.; Xu, T.; Li, C. Enhancing photocatalytic performance of heterostructure $MoS_2$/g-$C_3N_4$ embeded in PAN frameworks by electrospining process. *Mater. Sci. Semicond. Process.* **2021**, *121*, 105414. [CrossRef]
44. Bode-Aluko, C.A.; Pereao, O.; Kyaw, H.H.; Al-Naamani, L.; Al-Abri, M.Z.; Myint, M.T.Z.; Rossouw, A.; Fatoba, O.; Petrik, L.; Dobretsov, S. Photocatalytic and antifouling properties of electrospun $TiO_2$ polyacrylonitrile composite nanofibers under visible light. *Mater. Sci. Eng. B* **2021**, *264*, 114913. [CrossRef]
45. Cui, Y.; Jiang, Z.; Xu, C.; Zhu, M.; Li, W.; Wang, C. Preparation, filtration, and photocatalytic properties of PAN@g-$C_3N_4$ fibrous membranes by electrospinning. *RSC Adv.* **2021**, *11*, 19579–19586. [CrossRef]
46. Dai, K.; Lu, L.; Liang, C.; Liu, Q.; Zhu, G. Heterojunction of facet coupled g-$C_3N_4$/surface-fluorinated $TiO_2$ nanosheets for organic pollutants degradation under visible led light irradiation. *Appl. Catal. B* **2014**, *156*, 331–340. [CrossRef]
47. Chu, K.; Liu, Y.-p.; Li, Y.-b.; Guo, Y.-l.; Tian, Y. Two-dimensional (2D)/2D interface engineering of a $MoS_2/C_3N_4$ heterostructure for promoted electrocatalytic nitrogen fixation. *ACS Appl. Mater. Interfaces* **2020**, *12*, 7081–7090. [CrossRef]
48. Shafiee, A.; Aibaghi, B.; Carrier, A.J.; Ehsan, M.F.; Nganou, C.; Zhang, X.; Oakes, K.D. Rapid photodegradation mechanism enabled by broad-spectrum absorbing black anatase and reduced graphene oxide nanocomposites. *Appl. Surf. Sci.* **2022**, *575*, 151718. [CrossRef]
49. Yuangpho, N.; Trinh, D.T.T.; Channei, D.; Khanitchaidecha, W.; Nakaruk, A. The influence of experimental conditions on photocatalytic degradation of methylene blue using titanium dioxide particle. *J. Aust. Ceram. Soc.* **2018**, *54*, 557–564. [CrossRef]
50. Liu, M.; Zhao, L.; Gong, G.; Zhang, L.; Shi, L.; Dai, J.; Han, Y.; Wu, Y.; Khalil, M.M.; Sun, L. Invited review: Remediation strategies for mycotoxin control in feed. *J. Anim. Sci. Biotechnol.* **2022**, *13*, 19. [CrossRef]
51. Samuel, M.S.; Mohanraj, K.; Chandrasekar, N.; Balaji, R.; Selvarajan, E. Synthesis of recyclable GO/$Cu_3(BTC)_2/Fe_3O_4$ hybrid nanocomposites with enhanced photocatalytic degradation of aflatoxin $B_1$. *Chemosphere* **2022**, *291*, 132684. [CrossRef]
52. Li, Y.; Wang, Z.; Zhao, H.; Yang, M. Composite of $TiO_2$ nanoparticles and carbon nanotubes loaded on poly (methyl methacrylate) nanofibers: Preparation and photocatalytic performance. *Synth. Met.* **2020**, *269*, 116529. [CrossRef]
53. Li, J.; Liu, E.; Ma, Y.; Hu, X.; Wan, J.; Sun, L.; Fan, J. Synthesis of $MoS_2$/g-$C_3N_4$ nanosheets as 2D heterojunction photocatalysts with enhanced visible light activity. *Appl. Surf. Sci.* **2016**, *364*, 694–702. [CrossRef]
54. Samsudin, M.F.R.; Frebillot, C.; Kaddoury, Y.; Sufian, S.; Ong, W.-J. Bifunctional Z-scheme Ag/$AgVO_3$/g-$C_3C_4$ photocatalysts for expired ciprofloxacin degradation and hydrogen production from natural rainwater without using scavengers. *J. Environ. Manag.* **2020**, *270*, 110803. [CrossRef]
55. Fujishima, A.; Zhang, X.; Tryk, D.A. $TiO_2$ photocatalysis and related surface phenomena. *Surf. Sci. Rep.* **2008**, *63*, 515–582. [CrossRef]